Nanoscale

PAPER

View Article Online
View Journal | View Issue

Cite this: *Nanoscale*, 2023, **15**, 7077

Origin of the spectral red-shift and polarization patterns of self-assembled InGaN nanostructures on GaN nanowires

Maximilian Ries,[a,b] Felix Nippert,[a] Benjamin März,[c,d] Manuel Alonso-Orts,[e] Tim Grieb,[e,f] Rudolfo Hötzel,[e] Pascal Hille,[e] Pouria Emtenani,[a] Eser Metin Akinoglu,[b] Eugen Speiser,[b] Julian Plaickner,[b,g] Jörg Schörmann,[h] Matthias Auf der Maur,[i] Knut Müller-Caspary,[d] Andreas Rosenauer,[e,f] Norbert Esser,[a,b] Martin Eickhoff[e] and Markus R. Wagner *[a,j]

The luminescence of $In_xGa_{1-x}N$ nanowires (NWs) is frequently reported with large red-shifts as compared to the theoretical value expected from the average In content. Both compositional fluctuations and radial built-in fields were considered accountable for this effect, depending on the size, structure, composition, and surrounding medium of the NWs. In the present work, the emission properties of InGaN/GaN NWs grown by plasma-assisted molecular beam epitaxy are investigated in a comprehensive study combining ultraviolet-Raman and photoluminescence spectroscopy (PL) on vertical arrays, polarization-dependent PL on bundles of a few NWs, scanning transmission electron microscopy, energy-dispersive X-ray spectroscopy, and calculations of the band profiles. The roles of inhomogeneous In distribution and radial fields in the context of optical emission properties are addressed. The radial built-in fields are found to be modest, with a maximum surface band bending below 350 meV. On the other hand, variations in the local In content have been observed that give rise to potential fluctuations whose impact on the emission properties is shown to prevail over band-bending effects. Two luminescence bands with large positive and moderate negative polarization ratios of ≈+80% and ≤−60%, respectively, were observed. The red-shift in the luminescence is associated with In-rich inclusions in the NWs due to thermodynamic decomposition during growth. The negative polarization anisotropy is suggested to result from spontaneously formed superlattices in the In-rich regions of the NWs. The NWs show a preferred orthogonal absorption due to the dielectric boundary conditions and highlight the extreme sensitivity of these structures towards light polarization.

Received 5th October 2022,
Accepted 8th March 2023

DOI: 10.1039/d2nr05529e

rsc.li/nanoscale

[a]*Technische Universität Berlin, Institut für Festkörperphysik, Hardenbergstraße 36, 10623 Berlin, Germany. E-mail: markus.wagner@physik.tu-berlin.de*
[b]*Leibniz-Institut für Analytische Wissenschaften – ISAS e.V., Department Interface Analytics, Schwarzschildstraße 8, 12489 Berlin, Germany*
[c]*Ernst-Ruska-Centre for Microscopy and Spectroscopy with Electrons at Forschungszentrum Jülich, Wilhelm-Johnen-Str., 52425 Jülich, Germany*
[d]*Department of Chemistry and Center for NanoScience, Ludwig-Maximilians-Universität München, Butenandtstr. 11, 81377 Munich, Germany*
[e]*Universität Bremen, Institut für Festkörperphysik, Otto-Hahn-Allee 1, 28359 Bremen, Germany*
[f]*Universität Bremen, MAPEX Center for Materials and Processes, Bibliothekstr. 1, 28359 Bremen, Germany*
[g]*Helmholtz-Zentrum Berlin für Materialien und Energie GmbH, Hahn-Meitner-Platz 1, 14109 Berlin, Germany*
[h]*Justus-Liebig-Universität Gießen, I. Physikalisches Institut und Zentrum für Materialforschung (LaMa), Heinrich-Buff-Ring 16, 35392 Gießen, Germany*
[i]*University of Rome Tor Vergata, Department of Electronic Engineering, Via del Politecnico 1, 00133 Rome, Italy*
[j]*Paul-Drude-Institut für Festkörperelektronik, Leibniz-Institut im Forschungsverbund Berlin e.V., Hausvogteiplatz 5–7, 10117 Berlin, Germany*

1. Introduction

Semiconductor nanowires (NWs) have become a vivid field of research in the last two decades. A large variety of different growth techniques in combination with their promising properties, such as high crystalline quality,[1] one-dimensionality,[2] and variability for functionalization, makes semiconductor NWs interesting for a wide field of applications ranging from transistors and solar energy harvesting,[3] light-emitting diodes and laser diodes,[1,4–6] to photodetectors, waveguides,[4,7] and optochemical sensors.[8–10] Group-III–V NWs have attracted particular interest due to the tunability of the direct bandgap and improved material quality compared to bulk materials.[1,11] It has been shown that InGaN NW light-emitting diodes exhibit a reduced Auger recombination rate, *i.e.*, a lower efficiency droop,[3] compared to bulk InGaN or InGaN quantum wells (QWs).

Owing to the crystal symmetry and peculiarities of the geometry, luminescence emitted from semiconductor NWs exhi-

bits a distinct polarization dependence, which can be of importance for their application in single photon emitters and in imaging and display technologies.[4,12] The depolarization ratio ρ compares the intensities of parallel ($I_{\parallel}$) and orthogonally ($I_{\perp}$) polarized emissions with respect to the NW axis:

$$\rho = \frac{I_{\parallel} - I_{\perp}}{I_{\parallel} + I_{\perp}}. \quad (1)$$

In the case of group-III nitrides, polarization anisotropy has been found in both photoluminescence (PL) and electroluminescence measurements of pure GaN NWs and those with embedded InGaN nanodiscs (NDs).[5,13–16] Interestingly, these anisotropies contradict the expected ratio from the dipole selection rules of excitonic transitions.

Two main mechanisms have been identified to be of relevance for the polarization anisotropy in quasi-one-dimensional sample geometries: (i) quantum-mechanical confinement and (ii) dielectric confinement.[2] The latter leads to a preponderating emission of light with polarization along the nanowire axis and a positive ρ. The contribution of these effects is mainly based on the diameter of the respective NW and the dielectric contrast between the NW and the surrounding medium. As a rule of thumb, once the actual diameter of the NW exceeds the exciton Bohr radius, the first effect drastically weakens. For InGaN, the exciton Bohr radius is commonly expected to be around 3–10 nm, depending on the In content.[17] For NWs of larger diameter, the second, purely classical effect dominates, until the NW diameter becomes large enough to be comparable to bulk material.[2] Depolarization ratios of GaN NWs with embedded InGaN QWs[5,18–23] and quantum dots (QDs) have been frequently reported,[12,24–26] but not for InGaN NWs. Especially in structures containing QDs in a wire, *i.e.*, embedded regions that act as QDs, the emission properties can differ strongly due to non- or semi-polar side-facets and the emission typically shows polarization perpendicular to the NW axis.[24,25]

This study reports the composition, influence of radial electric fields, and polarization anisotropy of luminescence light emitted from $In_xGa_{1-x}N$ NWs grown on top of GaN NWs in a self-assembled process. The PL energy differs significantly from what is expected for the average In concentration as determined by X-ray diffraction (XRD) analysis. The origin of this red-shift is discussed with respect to compositional fluctuations and band-bending effects. The depolarization ratio reaches values as high as +90% at approximately 2 eV. An additional higher energy luminescence band is observed that exhibits a negative ρ. The origin of this band is addressed, and experimentally observed higher intensities for excitation with polarization perpendicular to the NW axis are discussed.

2. Results and discussion

This work reports measurements on two different kinds of samples: (i) as-grown, vertically-aligned arrays of NWs and (ii) bundles of a few NWs isolated from the as-grown samples. Scanning electron microscopy analysis of the as-grown GaN NWs reveals lengths of 1400 nm in total. In the base region they exhibit a diameter of 30 nm and growth proceeds along the $[000\bar{1}]$ direction. With increasing lengths, the coalescence between neighboring wires increases. For the as-grown GaN NW array, the average diameter of coalesced wires at the top is 80 ± 10 nm. The GaN base part in InGaN/GaN NW arrays has a length of ≈1100 nm. The InGaN part is grown on top with a length of approximately 370 nm. The growth details of the base part are identical to those of GaN NWs and can be found in the Experimental section. For the InGaN part, the diameter gradually increases to 110 ± 10 nm towards the top.

The following discussion is divided into four sections: (i) PL and Raman measurements of the as-grown vertically aligned NW arrays, (ii) PL experiments on bundles of a few NWs, (iii) scanning transmission electron microscopy (STEM) and energy-dispersive X-ray spectroscopy (EDX) analysis, and (iv) calculations of band bending.

2.1. Photoluminescence and Raman spectra of vertically aligned arrays

In Fig. 1, room-temperature PL spectra of the as-grown InGaN/GaN NW arrays (blue) are compared to the luminescence of GaN NWs (red). The GaN spectrum is characterized by the bandgap luminescence at 3.4 eV. The spectra of InGaN/GaN NWs exhibit a broad emission band between 2.0 and 2.8 eV. Such a broad PL emission band in the visible range indicates an inhomogeneous In distribution in the NWs and differences from one NW to the other. The peak position of the dominating band corresponds to an In content of 25–30%.[27]

On the same two samples, ultraviolet (UV)-Raman spectroscopy was performed. The first-order modes observed for the as-grown GaN NWs in Fig. 2(a) are the E_2(high) at 567 cm^{-1} and the longitudinal optical (LO) phonon A_1(LO) at 718 cm^{-1}; see also Table 1. The E_2(high) frequencies are close to the literature value of strain-free GaN (568 cm^{-1}).[28]

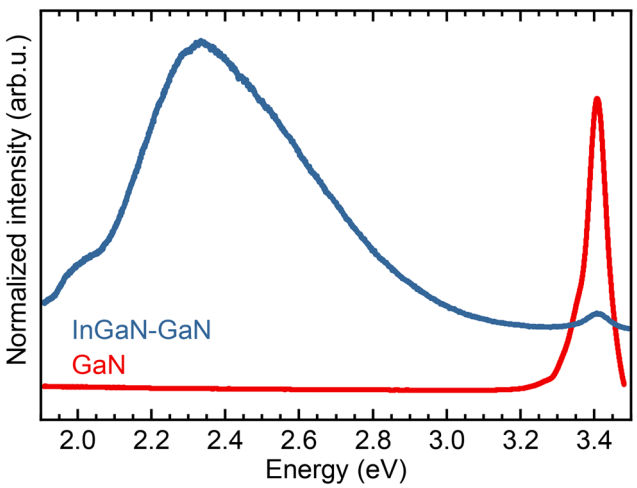

Fig. 1 Photoluminescence spectra of the as-grown GaN and InGaN/GaN NW ensembles recorded at 300 K. The spectra are offset for clarity.

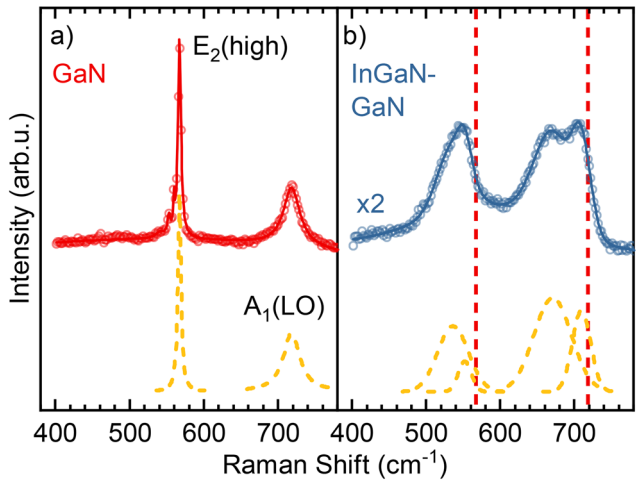

Fig. 2 UV-Raman spectra recorded from (a) the as-grown GaN (red) and (b) the as-grown InGaN/GaN NWs (blue) at 300 K. The yellow dashed lines indicate the individual fit components and the solid lines indicate the corresponding fits. Red vertical broken lines correspond to the position of the GaN NW E_2(high) and A_1(LO), respectively. The InGaN/GaN NW spectrum has been corrected by a Gaussian contribution to the background.

Table 1 Raman active modes from the as-grown GaN and InGaN/GaN NWs for 266 nm (UV) excitation; see Fig. 2 and references

	E_2 (high)		A_1 (LO)	
Sample	cm^{-1}		cm^{-1}	
GaN		567		718
InGaN/GaN	536	552	671	710
Ref. 28 and 33		568		734

However, the A_1(LO) shifts significantly from the expected position at 734 cm^{-1}.[28] The shift of the NW Raman modes to lower wavenumbers compared to bulk data is a result of phonon confinement,[29–31] and of excitation above the fundamental bandgap energy.[32] The NW sidewalls form boundaries that confine the phonons and lead to uncertainty in the associated wavevector. The larger shift of A_1(LO) originates from the steeper slope in the phonon dispersion, whereas the E_2(high) dispersion is rather flat.[33]

UV-Raman spectra of the as-grown InGaN/GaN NWs in Fig. 2(b) are characterized by an E_2(high) peak at 552 cm^{-1} with low-frequency shoulders at 536 cm^{-1} and an A_1(LO) structure consisting of two peaks at 710 cm^{-1} and 671 cm^{-1}, respectively. Concerning the as-grown InGaN/GaN NWs, the excitation wavelength has strong implications on the scattering volume: photons with energy below the InGaN bandgap penetrate deep into the NW material, probing both the InGaN and GaN parts, while photons with 266 nm are mainly absorbed in the InGaN part.

The frequency shift of the ternary $In_xGa_{1-x}N$ NW E_2(high) at 552 cm^{-1} yields an In distribution centered at around $x \approx 22\%$.[34] Considering the enlarged diameter of the $In_xGa_{1-x}N$ wire segment, the frequency shift due to phonon confinement can be neglected, so the A_1(LO) phonon frequency of 710 cm^{-1} translates directly to a value of $x \approx 16\%$.[34] The differing values obtained from the E_2(high) and A_1(LO) phonon modes highlight the inhomogeneity of the material and the complexity to relate a Raman shift to an In content.

The low-frequency peak of the A_1(LO) structure at 671 cm^{-1} suggests the occurrence of $In_xGa_{1-x}N$ with a higher In content x, which is also indicated by a low-frequency shoulder of the E_2(high) at 532 cm^{-1}. Both peak positions yield $x \approx 40\%$.[34] Surface optical modes, providing another possible explanation for the low-frequency A_1(LO) peak, should be located significantly above the observed mode at 671 cm^{-1}, which is not the case.[35–37]

2.2. PL of isolated nanowire bundles

Fig. 3 presents the excitation power-dependent PL spectra of a bundle with more than ten InGaN/GaN NWs dispersed on a glass substrate. Each PL spectrum consists of a GaN part, peak (III), at around 3.4 eV, and an InGaN part between 1.8 eV and 2.6 eV. The latter band is composed of two contributions centered at around 2.0 and 2.3 eV, labeled (I) and (II), respectively. Each color represents a different excitation power, starting with 100% or at around 1.7 mW (blue) down to 1% (red). The GaN PL red-shifts with increasing excitation power density and resulting laser heating. A similar behavior is observed for the lower energy feature (I). The main peak (II) follows the opposite trend. Its transition energy increases, and the peak area saturates, most likely due to screening of the internal piezoelectric field by the photogenerated charge carriers. This implies that the screening overcompensates the temperature-dependent red-shift. This behavior is not expected from the homogeneous wires, but indicates the occurrence of compositional fluctuations.[38]

In the following, the polarization anisotropy of two different bundles with fewer than 10 NWs will be compared. The respective PL spectra are shown in Fig. 4 together with atomic force microscopy (AFM) images. The excitation power

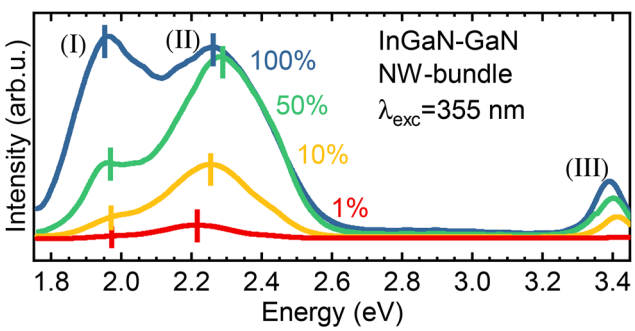

Fig. 3 Photoluminescence spectra recorded from an isolated InGaN/GaN bundle dispersed on a glass substrate at 300 K, excited with different power densities at 355 nm, where 100% corresponds to a laser power of ≈1.7 mW on the sample. The luminescence bands are labeled by Roman numbers and the respective peak positions are marked by vertical bars.

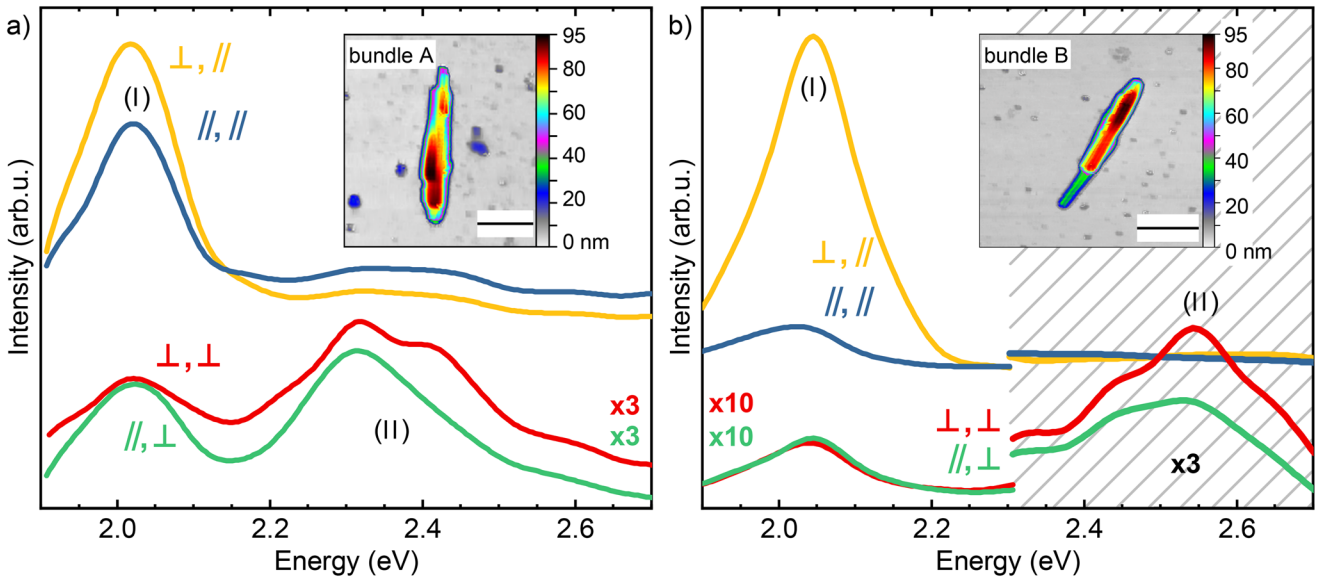

Fig. 4 Polarized PL spectra from two InGaN/GaN NW bundles (bundle A in (a) and bundle B in (b)) on silicon in the 1.9–2.7 eV range for 355 nm laser excitation at room temperature. The spectra are offset for clarity, and a Savitzky–Golay filter was applied. The polarization (*X*,*Y*) was controlled for both incoming (*X*) and outgoing light (*Y*) either parallel (||) or orthogonal (⊥) to the wire. The laser power was set to ≈1 mW. The insets show the AFM height profiles of the respective bundles. The scale bars represent 500 nm. Note that the *y*-axis for orthogonal collection is magnified by a factor of 3 in (a) and 10 in (b), while the gray hatched part in (b) is magnified by an additional factor of 3.

was approximately 1 mW and corresponds to 75% in Fig. 3. The depolarization ratio is mainly determined by the emission properties. Although the polarization anisotropy is stronger in perpendicular absorption and less prominent in the parallel case, as summarized in Table 2, the sign of the ratio is determined by the emission rather than the absorption. The difference in the depolarization ratio for perpendicular or parallel excitation, *i.e.*, absorption, can be ascribed to the dielectric boundary conditions and is extremely sensitive to the diameter, refractive indices, and wavelength.[2]

The InGaN-related part of both bundles exhibits two peaks. They have a dominating emission at around 2.0 eV, band (I), with a high mean depolarization ratio $\bar{\rho}$ of up to 80% and a second emission band (II) at around 2.2–2.6 eV with a moderate negative $\bar{\rho}$ below −60%, the latter being hardly noticeable in bundle B. The mean depolarization ratio is the average value from the two excitation polarizations. It is important to note that the excitation energy of 3.4 eV determines the absorption anisotropy, while the respective PL energy yields the emission anisotropy, *i.e.*, 2.0–2.6 eV. The structures of the two bundles are different. From the AFM insets, one can see that bundle B consists of at least two wires that are coalesced around the center. The bundle A in Fig. 4(a) has the same height, but the structure is less clear. The elevated part presumably at the bottom segment indicates additional NWs in this bundle.

In most reported cases on polar NWs, the luminescence is strongly polarized parallel to the NW axis, *i.e.*, $\rho \gg 0$.[5,12,22] In this case, this is true for band (I), but the depolarization ratio of the higher energy band (II) is negative. Chen *et al.* ascribed the reduced depolarization ratio for thicker, *i.e.*, coalesced GaN NWs to defect-related emission from localized excitons, rather than from free exciton emission.[15] This reflects well the geometry of the NWs studied in this publication. However, it only explains a reduced $\bar{\rho}$ from one wire to another, but not the change in sign.

A possible origin is the existence of QD-like formations in the NWs, *e.g.*, confined In-rich regions. It is well known from the literature that the so-called QDs in a wire structures can exhibit large negative polarization anisotropy.[12,24,25] This possible assignment is supported by Raman measurements, indicating localized regions with a high In content that most likely give rise to the low-frequency peak of the A_1(LO) structure, *cf.* Fig. 2.

Table 2 Depolarization ratios ρ and mean value $\bar{\rho}$ for the two bands observed in the polarized PL spectra (Fig. 4) for both excitation polarizations E_{exc}. The uncertainty of each peak area is estimated as 15% by comparing the GaN peak area between several measurements

Emission band	E (eV)	E_{exc}	Bundle A ρ	Bundle A $\bar{\rho}$	Bundle B ρ	Bundle B $\bar{\rho}$
(I)	2.0 eV	∥	37	51 ± 11	64	80 ± 5
		⊥	65		96	
(II)	2.2–2.6 eV	∥	−36	−56 ± 10	−33	−34 ± 13
		⊥	−75		−35	

2.3. STEM and EDX analyses

STEM analyses show that not all NWs are identical. They differ in length, diameter, and degree of coalescence. From comparative measurements we conclude that the In content is also not

the same in every NW.[39] However, there are characteristics that occur in the vast majority of NWs, which are well represented by the example shown in the annular-dark field STEM (ADF-STEM) image in Fig. 5. The diameter increases from about 30 nm at the GaN base to 80–100 nm at the InGaN part for a typical NW. The NWs in Fig. 5(a) show inclusions of brighter intensity that can be attributed to a region with a higher In concentration. This InGaN inclusion is surrounded by a shell, as can be seen by the slightly darker ADF intensity around the inclusion. Furthermore, STEM analysis revealed no change in the crystal structure for this region compared to the rest of the NWs. In the shell, no significant amount of indium was found by EDX. Towards the apex, the In concentration in the NWs increases to 30–40%.

The implication from Fig. 5(b) is that the measured In concentration decreases with increasing distance from the apex. These observations are supported by the results from Raman measurements, revealing a high In content and a low In-content phase, respectively. However, the concentration gradient seen by EDX is largely due to the fact that the width of the GaN shell increases towards the base of the NWs, which leads to an effective reduction of the In content measured with EDX.

Fig. 5(c) shows an ADF-STEM image of the upper part of the NWs in Fig. 5(a). It reveals an inner structure of the In-containing inclusion consisting of brighter and darker layers with a periodicity of about 2.2 nm. The high contrast in ADF-STEM images suggests a higher In content based on two mechanisms: (i) the contrast strongly depends on the material's atomic number (Z-contrast) and (ii) static disorder affects electron scattering significantly. An EDX intensity map from the region inside the black rectangle in Fig. 5(c) is shown in Fig. 5(d) with the intensities of the In–L and Ga–K lines color-coded. From the profile in Fig. 5(e) it is discernible that bright layers in the ADF image contain more indium compared to the darker layers. Due to a broadening of the STEM beam in the rather thick specimen and dynamical scattering effects, assigning an absolute composition to the EDX signal is a challenge that lies beyond the scope of the current study. However, it can be concluded that the In content fluctuates across the layers periodically, complementary to the Ga-content. The two characteristic features marked by arrows in Fig. 5(c) and Fig. 5(d) are stacking faults. The STEM analysis proves the presence of a superlattice that is not related to defects, but defects were observed especially in the upper half of the wires.

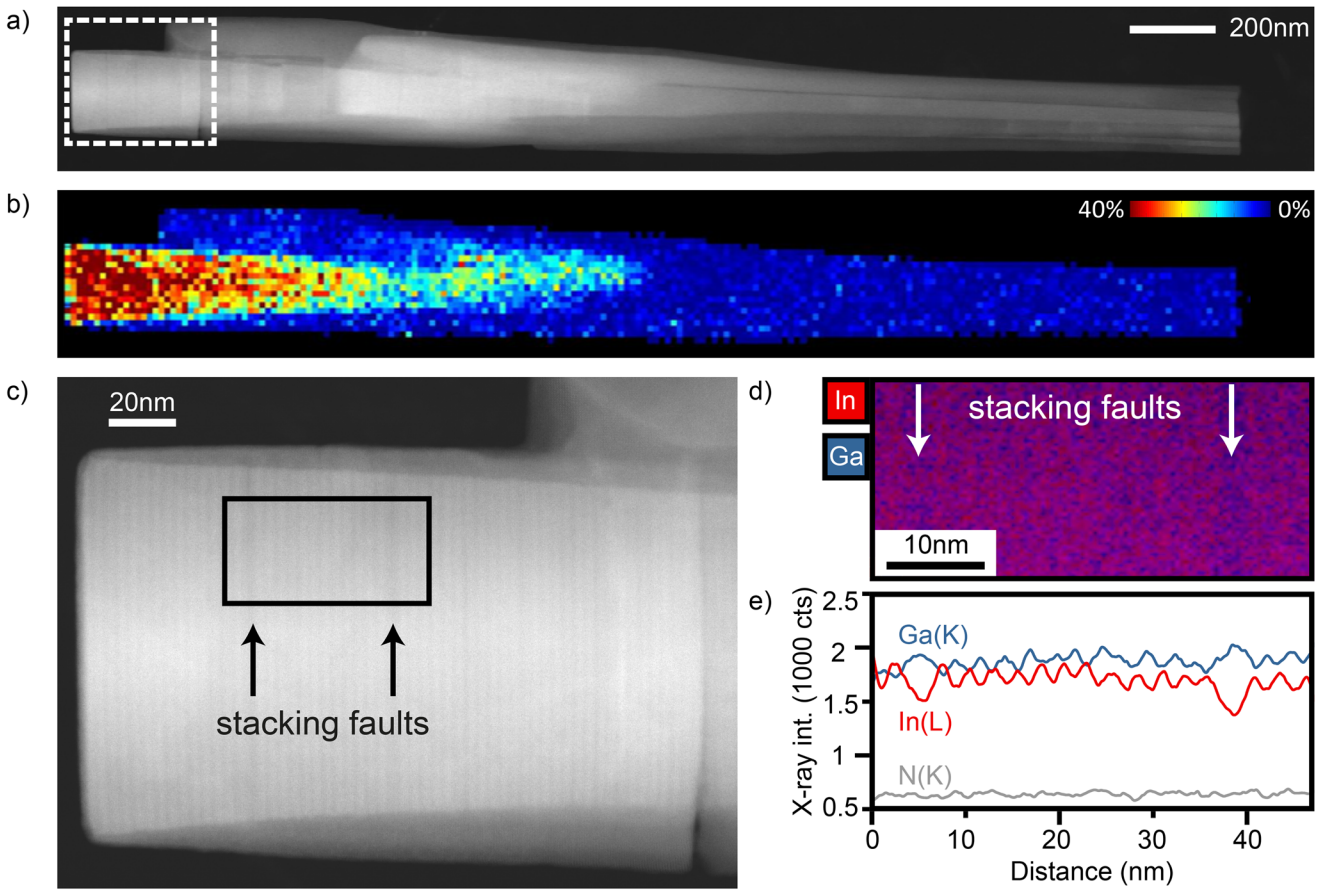

Fig. 5 (a) ADF-STEM image of InGaN/GaN NWs. (b) In concentration from EDX (with In + Ga = 100%). (c) Details of the top part (white box) of the NW in (a). The two characteristic stacking faults are marked by black arrows. (d) Integrated high-resolution EDX peak intensities from the region in the black rectangle in (c). Color-code: In L lines – red; Ga K lines – blue. (e) Ga(K), In(L), and N(K) profiles from averaging the map in (d).

In general, the NWs comprise the GaN base and the InGaN part, starting at the InGaN/GaN interface. This part is surrounded by a very thin GaN shell. The superlattice can be situated in between two InGaN parts or directly starting at the interface. In some cases, the top part is missing; however, this can be due as well to the dispersion of the nanowires *via* ultrasonication.

2.4. Calculations

To elucidate whether In-rich inclusions or surface-band-bending effects lead to a large luminescence red-shift, we performed band energy calculations at different doping levels.

Fig. 6 depicts the calculated profiles of the lowest conduction and the top-most valence band edges along the diameter in single freestanding InGaN/GaN NWs with a nominal In concentration of 30%. Inclined sidewalls with increasing diameter towards the top in combination with the growth direction $(000\bar{1})$ lead to a discontinuity of the normal component of the polarization field across the side surface, inducing an equivalent negative surface charge. Bulk doping with a density above 1×10^{17} cm^{-3} compensates for the polarization-induced surface charge, which becomes apparent from the realignment of the Fermi energy, as shown in Fig. 6(a).

The strain at the GaN–InGaN interface relaxes after <50 nm in both directions, thus piezoelectric effects exist only close to the interface. Consequently, the radial field close to the interface is slightly stronger compared to the center of the InGaN part. For low and moderate doping levels, the radial field is very small. Based on typical values for $n_e \approx 0.1$–1.0×10^{18} cm^{-3},[39,41,42] the radial electric field induces a band bending of less than 200 meV (for $In_{0.1}Ga_{0.9}N$/GaN NWs less than 350 meV), *i.e.*, it can not explain the observed red-shift of the luminescence, which enforces the suggested existence of In-rich regions.

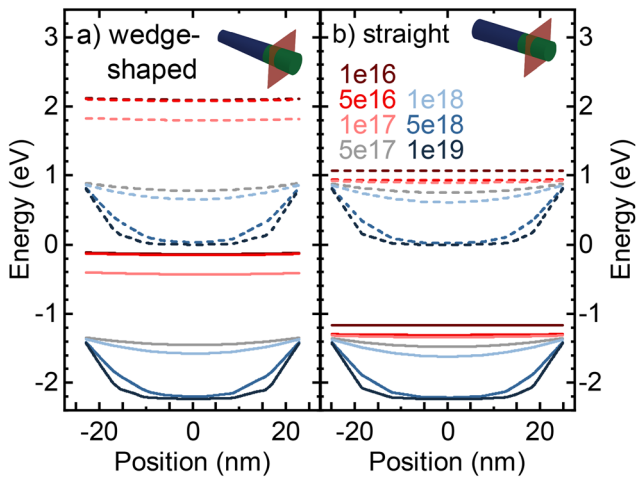

Fig. 6 Calculations of the valence (solid lines) and conduction band energies (broken lines) for different doping concentrations of 1×10^{16}–1×10^{19} cm^{-3} in (a) tapered (left) and (b) straight (right) $In_{0.3}Ga_{0.7}N$/GaN NWs. The density of the surface states was assumed to be 6×10^{14} cm^{-2} at energies consistent with Segev *et al.*[40] The NWs are assumed to be in air without surrounding electric fields. The insets show where the band profiles are extracted: 800 nm from the GaN base (blue), in the middle of the InGaN part (green). The intersection is visualized by a red plane.

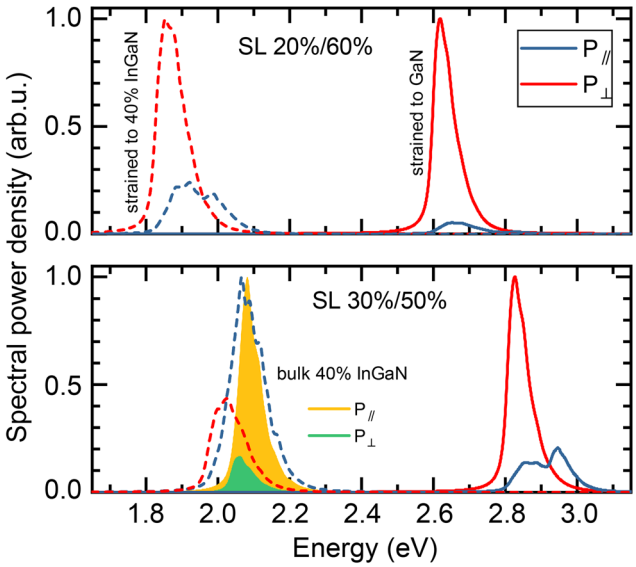

Fig. 7 1D-simulations of the spectral power density parallel and orthogonal to the NW *c*-axis in the electric-field approximation of a 20%/60%-InGaN superlattice (top) and a 30%/50%-InGaN superlattice (bottom) strained to 40%-InGaN and GaN, respectively. In the bottom panel, the yellow/green shaded areas correspond to bulk 40%-InGaN.

1D 8-band k·p simulation results of superlattices with alternating layers of 40%/60%-InGaN and 30%/50%-InGaN as shown in Fig. 7 underline the effect of strain on the emission characteristics of such structures. Both emission energy and dominant polarization depend crucially on the strain state of the nanowire due to the strain-induced band shifts. Fully strained to a surrounding GaN matrix, the orthogonal polarization dominates over the parallel case and the photoluminescence is strongly blue-shifted compared to the relaxed case (here 40%-InGaN). Furthermore, the emission characteristics approach those of the bulk case (yellow and green shaded areas) when the relaxation increases.

3. Conclusions

We have presented a comprehensive study of the structural and optical properties of InGaN nanostructures grown on GaN nanowires. By comparing the polarized PL spectra to the STEM images in Fig. 5, we have demonstrated that the emission band (I) originates predominantly from the top part of the NW, while the emission band (II) is caused by the superlattice emission surrounded by a GaN matrix from the part closer to the InGaN/GaN interface. The superlattices are not related to defects, but seem to originate from thermodynamic decomposition and inhomogeneous In incorporation during growth. Summarizing the obtained results by PL, Raman, and STEM-EDX measurements, as well as band-energy calculations,

we have presented evidence that surface band bending and a concomitant radial Stark effect play inferior roles in the observed red-shift of the luminescence of $In_xGa_{1-x}N$ NWs; instead, the dominating reason is the inhomogeneous In incorporation during growth that can spontaneously form superlattices. Furthermore, we have demonstrated that a pronounced polarization anisotropy of the emission is most likely related to the formation of superlattice structures.

4. Experimental

InGaN/GaN NWs were grown in high-density vertical arrays by plasma-assisted molecular beam epitaxy on n-type Si(111) substrates using a self-assembled-growth process under nitrogen-rich conditions.[43,44] The NWs exhibit a hexagonal cross-section, corresponding to the wurtzite crystal structure with growth direction along the $(000\bar{1})$ direction.[45] The NW density in the vertical arrays is in the order of 5–10 × 10^9 cm^{-2}. According to the PL data of single NWs previously reported[39] and, in comparison with reports from other groups, the charge carrier density in the InGaN/GaN NWs can be assumed to be around $n_e \approx 0.1–1.0 \times 10^{18}$ cm^{-3}.[39,41,42] The substrate temperatures during GaN growth were 770 °C and 520 °C during InGaN growth. Growth times were set to 90 min for the GaN base and 60 min for the InGaN part. Pure GaN NW arrays were grown similarly without the InGaN part. Single wires/small bundles were released by ultrasonication of the as-grown NWs in isopropanol for 60 s. The dispersed NWs were drop-cast onto specific substrates (natively oxidized Si(111) and glass) and identified by AFM measurements using a Park XE-100. Prior to PL measurements, the bundles were located with laser scanning and matched with the positions extracted from AFM. After successful PL measurements, the nanowire bundles were again imaged by AFM to guarantee that no structural changes occurred during optical measurements.

ADF-STEM imaging and EDX map data acquisition were conducted at 200 kV using a Hitachi HF5000 field emission STEM equipped with a dual Ultim® Max silicon drift detector system from Oxford Instruments. An area of 50.1 nm × 26.1 nm was scanned at a step size of 57 pm. The data set was 8 × 8 binned before peak deconvolution and display. The line scan was reconstructed from the original map data with applied 4 × 4 binning and a smoothing factor of 5.

Raman and PL spectra in the UV region (266 nm, Nd:YAG) were recorded in a back-scattering configuration using a Horiba T64000 spectrometer in single grating mode with a thermoelectrically cooled Synapse charge-coupled device. A UV-optimized 2400 lines per mm holographic grating with a spectral resolution of 4(2) cm^{-1} at 266 nm served as a dispersing element. UV-Raman spectra were collected with an LMU-40X-UVB, NA = 0.5 objective from Thorlabs. The spectra were calibrated to the Raman bands of β-Ga_2O_3 and atmospheric N_2 and O_2.

PL measurements at 355 nm were recorded with an 1800 lines per mm grating. The spectral resolution was around 0.5 meV at 3.492 eV. A Zeiss LD EC Epiplan-Neofluar ×100 (NA = 0.75) objective was used to focus light on the sample with a spot-size below 500 nm confirmed by confocal lateral laser scanning over a NW. The polarization of the excitation was controlled with a $\lambda/2$-plate behind the laser. The polarization dependence of the beamsplitter was taken into account. The emission polarization was rotated using a Fresnel rhomb to match the preferred configuration of the grating. A Rochon prism served as an analyzer in front of the spectrometer. The choice of these polarizing elements ensured stable polarization conditions over the entire spectral range. Measurements were performed with polarization parallel or perpendicular to both incident laser and emitted PL light with respect to the NW axis.

The band profile in $In_{0.3}Ga_{0.7}N$–GaN NWs was calculated by solving the 3-dimensional nonlinear Poisson equation, discretized with a standard finite-element scheme, for different values of bulk n-type doping. No compositional fluctuations have been considered. Electron and hole densities were calculated based on the standard bulk expressions using strain-corrected 8-band bulk k·p to calculate band edge energies.[46] The strain was calculated using linear elasticity under natural (zero force) boundary conditions.[47] For the spontaneous and piezoelectric polarization, the nonlinear model described by Prodhomme *et al.* was applied.[48] In the Poisson equation, surface states with a density of 6 × 10^{14} cm^{-2} were used as boundary conditions with energy levels according to Segev *et al.*,[40] and assuming zero electric fields outside the NW. For the calculation of the spectra shown in Fig. 7, we have taken into account that the emission from a dipole oriented orthogonally to the nanowire is partly suppressed.[2] Assuming the case of a small nanowire and an optical relative permittivity of $\varepsilon_r \approx 6.2$, we reduced the orthogonal polarization by a factor of $4/(1+\varepsilon_r)^2 \approx 0.077$.

Conflicts of interest

There are no conflicts to declare.

Acknowledgements

The authors thank the Ministerium für Innovation, Wissenschaft und Forschung des Landes Nordrhein-Westfalen, the Senatsverwaltung für Wirtschaft, Technologie und Forschung des Landes Berlin, and the German Bundesministerium für Bildung und Forschung for funding. Part of the work was funded by the European Regional Development Fund (ERDF) in the project 1.8/07. Authors from Universität Bremen acknowledge the financial support of the DFG *via* projects EI 518-12/1 and RO 2057/16-1. M. R. gratefully acknowledges the support by SALSA, a graduate school of Excellence Initiative of the Deutsche Forschungsgemeinschaft (DFG), and the financial support of the DFG within the Collaborative Research Center 787 (SFB 787).

References

1 Q. Li, K. R. Westlake, M. H. Crawford, S. R. Lee, D. D. Koleske, J. J. Figiel, K. C. Cross, S. Fathololoumi, Z. Mi and G. T. Wang, *Opt. Express*, 2011, **19**, 25528.
2 H. E. Ruda and A. Shik, *J. Appl. Phys.*, 2006, **100**, 024314.
3 *Novel Compound Semiconductor Nanowires*, ed. F. Ishikawa and I. A. Buyanova, Pan Stanford Publishing Pte Ltd, 2017.
4 M. Tchernycheva, A. Messanvi, A. de Luna Bugallo, G. Jacopin, P. Lavenus, L. Rigutti, H. Zhang, Y. Halioua, F. H. Julien, J. Eymery and C. Durand, *Nano Lett.*, 2014, **14**, 3515–3520.
5 T. Zhi, T. Tao, B. Liu, Z. Zhuang, J. Dai, Y. Li, G. Zhang, Z. Xie, P. Chen and R. Zhang, *IEEE Photonics Technol. Lett.*, 2016, **28**, 721–724.
6 S. W. Eaton, A. Fu, A. B. Wong, C.-Z. Ning and P. Yang, *Nat. Rev. Mater.*, 2016, **1**, 16028.
7 R. Yan, D. Gargas and P. Yang, *Nat. Photonics*, 2009, **3**, 569–576.
8 J. Wallys, J. Teubert, F. Furtmayr, D. M. Hofmann and M. Eickhoff, *Nano Lett.*, 2012, **12**, 6180–6186.
9 S. Hölzel, M. V. Zyuzin, J. Wallys, E. Pouokam, J. Müßener, P. Hille, M. Diener, W. J. Parak and M. Eickhoff, *Adv. Funct. Mater.*, 2018, **28**, 1802503.
10 K. Maier, A. Helwig, G. Müller, P. Hille, J. Teubert and M. Eickhoff, *Nano Lett.*, 2017, **17**, 615–621.
11 T. Kuykendall, P. Ulrich, S. Aloni and P. Yang, *Nat. Mater.*, 2007, **6**, 951–956.
12 S. Deshpande, J. Heo, A. Das and P. Bhattacharya, *Nat. Commun.*, 2013, **4**, 1675.
13 L. Rigutti, M. Tchernycheva, A. D. L. Bugallo, G. Jacopin, F. H. Julien, F. Furtmayr, M. Stutzmann, M. Eickhoff, R. Songmuang and F. Fortuna, *Phys. Rev. B: Condens. Matter Mater. Phys.*, 2010, **81**, 045411.
14 J. B. Schlager, N. A. Sanford, K. A. Bertness, J. M. Barker, A. Roshko and P. T. Blanchard, *Appl. Phys. Lett.*, 2006, **88**, 213106.
15 H.-Y. Chen, Y.-C. Yang, H.-W. Lin, S.-C. Chang and S. Gwo, *Opt. Express*, 2008, **16**, 13465.
16 P. Corfdir, F. Feix, J. K. Zettler, S. Fernández-Garrido and O. Brandt, *New J. Phys.*, 2015, **17**, 033040.
17 *Indium Nitride and Related Alloys*, ed. T. Veal, C. McConville and W. Schaff, CRC Press, 2009.
18 J. C. Li, T. C. Lu, H. M. Huang, W. W. Chan, H. C. Kuo and S. C. Wang, *J. Appl. Phys.*, 2010, **108**, 063508.
19 C. Kölper, M. Sabathil, F. Römer, M. Mandl, M. Strassburg and B. Witzigmann, *Phys. Status Solidi A*, 2012, **209**, 2304–2312.
20 H.-M. Huang, T.-C. Lu, C.-Y. Chang, S.-C. Ling, W.-W. Chan, H.-C. Kuo and S.-C. Wang, *J. Lightwave Technol.*, 2011, **29**, 2761–2765.
21 M. Athanasiou, R. M. Smith, Y. Hou, Y. Zhang, Y. Gong and T. Wang, *Appl. Phys. Lett.*, 2015, **107**, 141110.
22 H. K. Park, S. W. Yoon, Y. J. Eo, W. W. Chung, G. Y. Yoo, J. H. Oh, K. N. Lee, W. Kim and Y. R. Do, *Sci. Rep.*, 2016, **6**, 28312.
23 Y. Park, C. C. S. Chan, L. Nuttall, T. J. Puchtler, R. A. Taylor, N. Kim, Y. Jo and H. Im, *Sci. Rep.*, 2018, **8**, 8124.
24 Y.-J. Lu, H.-W. Lin, H.-Y. Chen, Y.-C. Yang and S. Gwo, *Appl. Phys. Lett.*, 2011, **98**, 233101.
25 E. Chernysheva, Ž. Gačević, N. García-Lepetit, H. P. van der Meulen, M. Müller, F. Bertram, P. Veit, A. Torres-Pardo, J. M. G. Calbet, J. Christen, E. Calleja, J. M. Calleja and S. Lazić, *EPL*, 2015, **111**, 24001.
26 K. H. Li, Q. Wang, H. P. T. Nguyen, S. Zhao and Z. Mi, *Phys. Status Solidi A*, 2015, **212**, 941–946.
27 E. Sakalauskas, O. Tuna, A. Kraus, H. Bremers, U. Rossow, C. Giesen, M. Heuken, A. Hangleiter, G. Gobsch and R. Goldhahn, *Phys. Status Solidi B*, 2012, **249**, 485–488.
28 H. Harima, *J. Phys.: Condens. Matter*, 2002, **14**, R967–R993.
29 H. Richter, Z. P. Wang and L. Ley, *Solid State Commun.*, 1981, **39**, 625–629.
30 R. J. Nemanich, S. A. Solin and R. M. Martin, *Phys. Rev. B: Condens. Matter Mater. Phys.*, 1981, **23**, 6348–6356.
31 H.-L. Liu, C.-C. Chen, C.-T. Chia, C.-C. Yeh, C.-H. Chen, M.-Y. Yu, S. Keller and S. P. DenBaars, *Chem. Phys. Lett.*, 2001, **345**, 245–251.
32 C. Kranert, R. Schmidt-Grund and M. Grundmann, *New J. Phys.*, 2013, **15**, 113048.
33 H. Siegle, G. Kaczmarczyk, L. Filippidis, A. P. Litvinchuk, A. Hoffmann and C. Thomsen, *Phys. Rev. B: Condens. Matter Mater. Phys.*, 1997, **55**, 7000–7004.
34 S. Hernández, R. Cuscó, D. Pastor, L. Artús, K. P. O'Donnell, R. W. Martin, I. M. Watson, Y. Nanishi and E. Calleja, *J. Appl. Phys.*, 2005, **98**, 013511.
35 R. Mata, A. Cros, K. Hestroffer and B. Daudin, *Phys. Rev. B: Condens. Matter Mater. Phys.*, 2012, **85**, 035322.
36 A. G. Kontos, Y. S. Raptis, N. T. Pelekanos, A. Georgakilas, E. Bellet-Amalric and D. Jalabert, *Phys. Rev. B: Condens. Matter Mater. Phys.*, 2005, **72**, 155336.
37 S.-E. Wu, S. Dhara, T.-H. Hsueh, Y.-F. Lai, C.-Y. Wang and C.-P. Liu, *J. Raman Spectrosc.*, 2009, **40**, 2044–2049.
38 K. D. Goodman, V. V. Protasenko, J. Verma, T. H. Kosel, H. G. Xing and D. Jena, *J. Appl. Phys.*, 2011, **109**, 084336.
39 T. Kehagias, G. P. Dimitrakopulos, P. Becker, J. Kioseoglou, F. Furtmayr, T. Koukoula, I. Häusler, A. Chernikov, S. Chatterjee, T. Karakostas, H.-M. Solowan, U. T. Schwarz, M. Eickhoff and P. Komninou, *Nanotechnology*, 2013, **24**, 435702.
40 D. Segev and C. G. Van de Walle, *Europhys. Lett.*, 2006, **76**, 305–311.
41 J. Lähnemann, P. Corfdir, F. Feix, J. Kamimura, T. Flissikowski, H. T. Grahn, L. Geelhaar and O. Brandt, *Nano Lett.*, 2016, **16**, 917–925.
42 R. Calarco, M. Marso, T. Richter, A. I. Aykanat, R. Meijers, A. V. D. Hart, T. Stoica and H. Lüth, *Nano Lett.*, 2005, **5**, 981–984.
43 P. Hille, F. Walther, P. Klement, J. Müßener, J. Schörmann, J. Kaupe, S. Mitić, N. W. Rosemann, S. Chatterjee, A. Beyer,

K. I. Gries, K. Volz and M. Eickhoff, *J. Appl. Phys.*, 2018, **124**, 165703.
44 P. Neuderth, P. Hille, J. Schörmann, A. Frank, C. Reitz, S. Martí-Sánchez, M. de la Mata, M. Coll, J. Arbiol, R. Marschall and M. Eickhoff, *J. Mater. Chem. A*, 2018, **6**, 565–573.
45 M. de la Mata, C. Magen, J. Gazquez, M. I. B. Utama, M. Heiss, S. Lopatin, F. Furtmayr, C. J. Fernández-Rojas, B. Peng, J. R. Morante, R. Rurali, M. Eickhoff, A. F. I. Morral, Q. Xiong and J. Arbiol, *Nano Lett.*, 2012, **12**, 2579–2586.
46 S. L. Chuang and C. Chang, *Phys. Rev. B: Condens. Matter Mater. Phys.*, 1996, **54**, 2491.
47 M. Povolotskyi and A. Di Carlo, *J. Appl. Phys.*, 2006, **100**, 063514.
48 P.-Y. Prodhomme, A. Beya-Wakata and G. Bester, *Phys. Rev. B: Condens. Matter Mater. Phys.*, 2013, **88**, 121304.